Element-specific cluster growth on the two-dimensional metal-organic network.

Noriyuki Tsukahara*[1,2], Ryuichi Arafune[3] and Jun Yoshinobu[2]

[1]*National Institute of Technology, Gunma College, Toriba-machi 580, Maebashi-shi, Gunma, 370-8530, Japan*

[2]*The institute for Solid State Physics (ISSP), The University of Tokyo, Kashiwanoha 5-1-5, Kashiwa-shi, Chiba, 277-8581, Japan*

[3]*International Center for Materials Nanoarchitectonics (WPI-MANA), National Institute for Materials Science (NIMS), Tsukuba, Ibaraki 304-0044, Japan*

E-mail: ntsukahara@gunma-ct.ac.jp

A porous two-dimensional metal-organic network (2D-MON) on the substrate captures deposited metal atoms and metal clusters grow in the pores of the 2D-MON. We found that the growth mechanisms of Ag, In, and Pd clusters in the 2D-MON synthesized from 1,3,5-tris(4-bromophenyl)benzene molecules on Ag(111) are different from each other, and the difference derives from the interaction of an adatom with the 2D-MON. Ag and Pd clusters grow from the 2D-MON since the interaction of Ag and Pd adatoms with the 2D-MON is attractive. In clusters grow inside of the pores of the 2D-MON since the interaction between an In adatom and the 2D-MON is repulsive. The growth process of metal clusters is determined by the element-specific behavior of metal adatoms in the pores, taking into account interactions with the 2D-MON.

1. Introduction

Solid surfaces provide a platform to fabricate various low-dimensional structures, and the formation of surface-supported two-dimensional metal-organic networks (2D-MONs) based on supramolecular chemistry is also achieved on the substrate.[1,2] Various 2D-MONs, that is, periodic structures of metal atoms and organic molecules that link the metal atoms (linker molecules), have been synthesized by supplying the metal atoms and the linker molecules onto the substrate. As far as we know, a 2D-MON by co-deposition of the Fe atoms and the 1,2,4-benzenetricarboxylic acid molecules on Cu(100) is the first reported example using this method.[3] In some cases, only linker molecules are adsorbed onto metal surfaces, and metal atoms are supplied from the substrate to form 2D-MONs.[4–10] The intermediate reaction product of the coupling reaction induced by a metal atom takes a "linker-metal-linker" structure, and the product on the substrate is also a kind of the 2D-MON.[11] Since the cohesive energy of metal-ligand coordination is about 0.2 ~ 2 eV, 2D-MONs are thermally more stable than other 2D supramolecular systems.[1] However, the formation of 2D-MONs is governed by the substrate,[12] and the interplay between the inter-adsorbate interaction and the adsorbate-substrate interaction is the key to forming the well-developed 2D-MONs. A 2D-MON of sub-micrometer scale is possible by the good commensurability.[13]

In addition to the properties of 2D-MONs such as the electronic states,[14–17] the magnetic properties,[18–21] and the catalytic functions,[22] porous 2D-MONs have a function that pores confine electrons in the substrate, adatoms, and adsorbed molecules. The Shockley surface state of Cu(111) and Ag(111) is confined by the pores, and standing waves are observed by scanning tunneling microscopy/spectroscopy (STM/STS).[23–26] The pores capture incoming guest atoms and molecules, and the 2D-MON works as the host layer. Although thermal energy induces the rotation and diffusion of the captured molecules on the surface, the pores keep enclosing the molecules even at finite temperature.[27,28] The electrons injected by scanning tunneling microscopy (STM) induce molecular motions inside of the pores.[29] For the Co-tetra-pyridyl-porphyrin molecules on Cu(111) and Au(111) surfaces, the spin state of the molecules is switched by introduction of the 2D-MON through the modulation of the molecule-substrate height,[30] indicating that tuning the adsorbate-substrate interaction is possible by the 2D-MON. The 2D-MON enable Fe and Bi adatoms to arrange self-assembled Fe and Bi nanoclusters in the pores,[24,31] and can be a template to grow self-assembled metal nanoclusters.

Growth of a metal cluster in a pore of the 2D-MON requires that the pore is a local minimum of the potential energy surface, that is, a potential well for the metal adatoms. By arranging nanometer-scale potential wells on the substrate, deposited metal atoms form metal nanoclusters spontaneously. An template for cluster growth is the moiré structure of the graphene on a well-defined metal substrate.[32–38] Ir, Rh, and Pt nanoclusters grow on the graphene moiré, and the origin of the potential well is the mixing between modulated C $2p_z$ orbitals by the substrate and d orbitals of the adatom.

As introduced above, porous 2D-MONs are another candidate for the template to grow metal nanoclusters. Although the interaction between adsorbed metal atoms in a pore of the 2D-MONs and the 2D-MONs is important to clarify the mechanism of metal cluster growth, it has not been considered yet. In this report, 1,3,5-tris(4-bromophenyl)benzene (TBB) molecules and Ag(111) are the precursors of the 2D-MON and the substrate, respectively. Silver (Ag), indium (In), and palladium (Pd) atoms are the guest atoms. We performed STM measurements and density functional theory (DFT) calculations to observe the differences in the interaction and aggregation process between Ag, In, and Pd adatoms and the 2D-MON, and discuss the mechanism.

2. Experimental and calculated methods

The details of preparing an Ag(111) surface grown on an Si(111) surface and depositing TBB molecules on the substrate were reported in our previous study.[39] Heating the substrate with 1 ML TBB molecules up to 400 K induces the dehalogenation reaction and a 2D-MON appears. In this procedure, isolated Br atoms remain on the substrate. The Ag and Pd evaporators are made of a W wire (ϕ0.2 mm) with an Ag and a Pd wires (ϕ0.15 mm) wrapped around the W wire. The indium evaporator is made of a Ta crucible bridged to the electrodes by W wires (ϕ0.2 mm), and In pieces are contained in the crucible. Ag, In, and Pd atoms are deposited onto the 2D-MON on Ag(111) by heating the evaporators with an electric current. The deposition rate was monitored by a thickness monitor and the coverage was controlled by the deposition time. The deposition procedure is as follows. (1) The substrate with the 2D-MON is cooled to approximately 80 K. (2) The substrate is transferred to a position in front of the evaporator by a room-temperature transfer rod, and metal atoms are deposited. (3) After the deposition, the substrate is returned to the cooling position. Steps (1) to (3) typically take about 20 ~ 30 seconds, and the substrate temperature is thought to have risen to about 100 K.

All the STM/STS experiments were performed in an ultrahigh-vacuum chamber with a low-temperature STM working at 78 K. All the STM images were acquired by constant-current mode with a bias voltage, V_s, applied to the sample. An electrochemically etched W wire (diameter of 0.3 mm) was used as an STM probe. The DFT calculations were performed by using the plane-wave-based Vienna Ab initio Simulation Package (VASP)[40] with the projected augmented wave (PAW) method.[41] Van der Waals interactions were included using the van der Waals density functional (vdW-DF) describing all nonlocal correlation energy, while the local correlation energy was described by local density approximation (LDA) and the exchange energy was described on the GGA level (optB86b-vdW functional).[42] For the calculation of the 2D-MON on Ag(111), a three-layered slab is separated by about 2.0 nm of vacuum in the surface unit cell. 2×2×1 k-point sampling with the Monkhorst-Pack method and a 400 eV kinetic energy cutoff were used. To obtain the optimal structure, structural relaxation was carried out under the condition that the forces acting on the atoms in the molecules and the two uppermost layers of the slabs were converged within 0.02 eV/Å.

3. Results and discussion

The structure of this chapter consists of four sections. First, in 3.1, the observed 2D-MON on Ag(111) using STM will be described. The section 3.2 is the main results in this paper, where the cluster formation of three different metal atoms (Ag, In, and Pd) in the 2D-MON will be reported in detail. In order to understand the interaction of these metal atoms with the 2D-MON, the results of DFT calculations will be presented in 3.3. In 3.4, the different behavior of cluster formation and its mechanism will be discussed based on both experimental and theoretical results.

3.1 2D-MON on Ag(111)

Figure 1 (a) is an STM image of 1 ML TBB molecules on Ag(111) after heating the substrate at 400 K. A two-dimensional network with mostly hexagonal pores is observed. A larger-scale STM image is shown in Figure S1 (a) in the supplementary data. From previous studies, the network structure is the product of the dehalogenation reaction, that is, a 2D-MON.[43–47] The length of the side of the hexagons is 14.9 Å and there is a faint protrusion at the center of the side as shown in Figure 1 (b) (line 1). The protrusion in line 1 correspond to the two-coordinated Ag atoms in the 2D-MON,[44,45,47] and Figure 1 (c) shows the schematic drawing of the 2D-MON along line 1. We call the two-coordinated Ag atom

Ag^{MON} in the present study. In rare cases, the length of the side is 12.2 Å, and there is no faint protrusion at the center as shown in Fig. 1 (b) (line 2). This derives from the C-C covalent bond as shown in Fig. 1 (c).[44,47] Although the shape of most pores is hexagonal, pores of other shapes also appear and the 2D-MON have low uniformity. Previous study shows that the C-Ag^{MON}-C bond is stable when bent without considering the substrate.[45] On the other hand, the C-Ag^{MON}-C bonds are linear in hexagonal pores, and the Ag(111) substrate constrains pores of the 2D-MON to be hexagonal. As a result, the 2D-MON is partially disturbed and both hexagonal and non-hexagonal pores appear.[45] In Fig. 1 (a), there are many small protrusions at the vertices of the pores. The small protrusions are assigned to be Br adatoms produced by the dehalogenation reaction. Similar protrusions are observed with other 2D-MONs synthesized by the dehalogenation reaction.[16,48] In a previous STM and XPS study of 1,3-bis(p-bromophenyl)-5-(p-iodophenyl)benzene on Ag(111), chemisorbed Br adatoms increase as the 2D-MON is formed upon heating, and the authors assigned the small protrusions to be Br adatoms.[44] In addition, the number of protrusions within a pore is 2.1 on average. As is explained later, when a hexagonal pore is formed, three Br adatoms should appear per pore. Some Br adatoms are confined in the pores, and others diffuse far away before the pore is formed. As a result, the number of Br adatoms in a pore is less than three on average. Figure 1 (d) shows the line profiles of the unconnected molecular lobes on lines 3 and 4 in Fig. 1 (a). The length from the molecular center to the terminal is mostly 12.2 Å, and is rarely 7.2 Å. From a previous study, these derive from halogenated and dehalogenated lobes as shown in Figure 1 (e).[44] In addition, it is also conceivable that the longer lobe is terminated by Ag^{MON} as shown in Fig. 1 (e). An enlarged STM image and the schematic drawing of the 2D-MON is shown in Figure 1 (f). Figures 1 (g) and (h) are models of the 2D-MON on Ag(111), and the structure is optimized by the DFT calculation. The length of the side of the hexagons is 15.3 Å, and agrees with the STM result in Figs. 1 (a) and 1 (b). The black parallelogram surrounding the pore is the unit cell, and the unit cell contains two dehalogenated molecules and three Ag^{MON}. Therefore, three Br adatoms appear when a hexagonal pore is formed. As shown in Fig. 1 (h), the distances of Ag^{MON} and the molecular center from the surface are 2.31 Å and 3.54 Å, respectively. Since the distance for an isolated Ag adatom on Ag(111) is 2.14 Å in the present calculated condition, the linkers cause Ag^{MON} to lift slightly from the Ag(111) surface in the vacuum direction.

3.2 Three types of metal clusters on the 2D-MON

Figures 2 (a), (b), and (c) show an STM image after deposition of Ag, In, and Pd atoms onto the 2D-MON, respectively. A large-scale STM images are also shown in the supplementary data (S1). After Ag, In, and Pd deposition, several protrusions with various size appear on the 2D-MON. Since the size of the protrusions has coverage dependence as shown in the supplementary data (S2), the protrusions in the STM images in Fig. 2 (a), (b), and (c) are Ag, In, and Pd clusters, respectively. The 2D-MON maintains its structure, including Br adatoms after Ag and In deposition. On the other hand, two unconnected lobes that are adjacent to each other appears after Pd deposition as indicated by dotted circles in Fig. 2 (c).

Ag clusters are classified into three types (labeled as α, β, and γ) based on the structure, and Figures 2 (d), (e), and (f) show line-profiles of the Ag clusters. Details of the line profiles and the structures of the Ag clusters are shown in the supplementary data (S3 and S4). Since the height of the α cluster, 3.08 Å, corresponds to the sum of the heights of one Ag layer (2 Å) and the 2D-MON (1 Å), α clusters are between the substrate and the 2D-MON (especially Ag^{MON}) and grow from the 2D-MON (Ag^{MON}). Since there is a gap between the β cluster and the 2D-MON as indicated by the blue arrow in Fig. 2 (e), β clusters grow in the pores of the 2D-MON and is not connected to the 2D-MON. The height of the β cluster, 2.28 Å, corresponds to that of one Ag layer. Since there is no gap between the cluster and the 2D-MON in the line-profile shown in Fig. 2 (f), γ clusters are connected to the 2D-MON. γ clusters grow from the unconnected lobes of the 2D-MON. The height of the γ cluster, 2.03 Å, corresponds to that of one Ag layer. Among the observed Ag clusters, α is the most numerous, followed by γ. β is rarely observed. If the 2D-MON has no terminals, most Ag clusters are considered to be α. Therefore, Ag clusters mainly grow from the 2D-MON (Ag^{MON}).

In clusters are classified into two types (β and γ) based on the line-profiles in Figures 2 (g) and (h) when classified in the same manner as Ag clusters. The heights of the noisy clusters are 1.8 to 1.9 Å, and those of the other clusters are 2.4 ~ 2.5 Å, and both are the height of one In layer. We think that noisy clusters are about to dissolve, and the height is similar to that of an In adatom, and similar noisy Bi clusters are observed in the previous study.[31] Stable clusters are considered to be more crystalline and show higher conductivity than noisy

clusters. If the 2D-MON has no unconnected lobes, most In clusters are considered to be β. Therefore, In clusters mainly grow in the pores. Note that ring-shaped protrusions in the pores are also observed as shown by the dotted circle in Fig. 2 (b).

Pd clusters at the terminal of the 2D-MON are γ, and the line-profile shown in Figure 2 (i) is similar to those in Figs. 2 (f) and (h). Other Pd clusters mainly grow at Ag^{MON} as shown by the dotted squares in Figs. 2 (c) (and S2 (e)). After deposition of Pd, many broken C-Ag^{MON}-C bonds appear. With increasing Pd coverage, Pd clusters appear between two molecules. Since Pd clusters are expected to grow from unconnected lobes that appear by broken C-Ag^{MON}-C bonds, these are also γ. Breaking Ag^{MON}-C bonds is expected to be due to highly reactive Pd adatoms for the coupling reaction.

As shown in Figs. 2 (a) and (b), isolated Ag and In adatoms are observed. Figures 3 (a) and (b) show enlarged images of the Ag and In adatoms, respectively. Since the Ag and In adatoms is at 6.6 Å and 4.0 Å from Ag^{MON}, respectively, significant orbital mixing does not occur, and it is discussed later by DFT calculation. Although Ag adatoms move by scanning as shown in Fig. 3 (a), it does not frequently occur compared to In adatoms. In adatoms frequently move in the pores during scanning. The interactions of Ag and In adatoms with the 2D-MON are attractive and not attractive, respectively. The behavior of the adatoms is related to cluster formation, and the detail is given in Section 3.4.

3.3 DFT calculations of Ag, In, and Pd adatoms in a pore

To understand the difference in growth mechanism between the Ag, In, and Pd clusters from the viewpoint of energy and electronic states, we have performed DFT calculations for an isolated Ag, In, and Pd adatom in a pore and clarify the behavior of the adatoms in a pore. Figure 4 (a) shows labels of the adsorption sites for Ag, In, and Pd adatoms. Figures 4 (b) to (d) shows the difference in the total energy of the 2D-MON with Ag, In, and Pd adatoms at each indicated site and that of the 2D-MON with an adatom at site A (the center of the pore), respectively. An Ag adatom at site K and an In adatom at site L are observed as shown in Figs. 3 (a) and (b), respectively. For the 2D-MON with an adatom (Ag at site K and A, In at site L, J and A), structural relaxation is performed, and the energy difference with structural relaxation is within a few meV from that without structural relaxation. For the 2D-MON

with a Pd adatom at site K, structural relaxation did not converge since the 2D-MON collapsed due to the strong interaction between the H atoms of the 2D-MON and the Pd adatom. The closer Ag and Pd adatoms are to the 2D-MON, the lower the energy, while the center of the pore is the lowest energy position for an In adatom. The energy difference in Figs. 4 (b) to (d) represents potential difference relative to site A. Ag and Pd adatoms receive attractive force from the 2D-MON, and an In adatom receives repulsive force from the 2D-MON. The energy differences between Ag, In, and Pd adatoms at site K and A, $E_K - E_A$, are -74.6, 66.6, and -227 meV, respectively. Since Ag and Pd clusters grow from the 2D-MON and In clusters grow in the pore, the calculated results are consistent with the STM results. Figures 4 (e) and (f) show the PDOS of Ag^{MON} without and with an Ag adatom at site K, respectively. PDOS of an Ag adatom on Ag(111) and at site K are also shown in Figs. 4 (e) and (f), respectively. The PDOS of Ag^{MON} in Fig. 4 (e) is exactly the same as that in Fig. 4 (f), and that of the Ag adatom at site K in Fig. 4 (f) is also similar to that of an Ag adatom on Ag(111) in Fig. 4 (e) (the slight difference in LDOS shape is derived from the calculated condition, such as k-point sampling). Therefore, orbital mixing between Ag^{MON} and an Ag adatom at site K is negligible. Similarly, in the case of In and Pd adatoms at site K, orbital mixing with Ag^{MON} does not occur. Other interactions such as the Coulomb interaction, the van der Waals interaction, and the interaction via the Ag substrate should be considered, which will be discussed later.

3.4 Discussion

The structure of Ag, In, and Pd clusters on the 2D-MON are mainly classified into α, β, and γ, respectively, and the growth mechanisms of the α, β, and γ clusters are determined by the interaction between an adatom and the 2D-MON. Since the interaction between Ag and Pd adatoms and the 2D-MON is attractive, the potential wells for these adatoms are located at the 2D-MON and clusters grow from the 2D-MON (α or γ). α clusters grow from the 2D-MON while maintaining the structure of the 2D-MON. γ clusters grow from unconnected lobes that are at the edge of the 2D-MON and appear by broken C-Ag^{MON}-C bonds. On the other hand, since the interaction between In adatoms and the 2D-MON is repulsive, the potential wells for the adatoms are located far from the 2D-MON, that is, the center of the pore, and In clusters grow in the pore (β).

We consider the origin of the interaction between Ag, In, and Pd adatoms and the 2D-MON. Since the adatoms interact with the 2D-MON even at a distance of about 1 nm as shown in Figs. 4 (b) to (d), the interaction is long-range forces. The net charge of Ag^{MON}, Ag, In, and Pd adatoms on Ag(111) are calculated by Bader charge analysis,[49–52] and the values are 0.23*e*, -0.01*e*, 0.38*e*, and -0.14*e*, respectively ($e = 1.6 \times 10^{-19}$ C). The detail of the Bader charge analysis for the 2D-MON is shown in supplementary data (S5). The repulsive (attractive) interaction between an In (a Pd) adatom and the 2D-MON is derived from Coulomb interaction, and $E_K - E_A$ in Figs. 4 (c) and (d) roughly agrees with the toy model shown in supplementary data (S6). As for an Ag adatom, since an Ag adatom is almost neutral on Ag(111), Coulomb interaction is negligible. A candidate for another attractive interaction is the van der Waals interaction. $E_K - E_A$ is 69.9 meV without vdW correction (-74.6 meV with vdW correction). In previous DFT studies for the interactions between atoms, molecules, and layered materials, van der Waals corrections for the exchange-correlation functional often give improved results compared to the results without van der Waals corrections.[42,53–55] Although careful comparison with other functionals is necessary, optB86b-vdW, which is used in the present study, is considered to give a good result and van der Waals interaction is a candidate for the attractive interaction between an Ag adatom and the 2D-MON. Considering that the polarizability is expected to be higher for Ag^{MON} than that of C or H atoms in the 2D-MON,[56] it is reasonable that Ag adatoms are mainly attracted to Ag^{MON} by the van der Waals interaction. Note that the calculated results for the In and Pd adatoms with optB86b-vdW and PBE functionals show the same tendency. The energies in Figs. 4 (b) to (d) does not show a monotonical increase or decrease. It is caused by the slight distortion of the Ag outer surface in the pore. Since the outer surface is slightly distorted, and we cannot carry out calculation with precisely same condition for sites A to K and errors appear in Figs. 4 (b) to (d).

Finally, we need to consider repulsive interaction between two adatoms for In and Pd due to non-zero net charge. As for In, there are many isolated adatoms and noisy (mobile) clusters. This is expected to be due to the repulsive interaction. As for Pd, adatoms approach the 2D-MON without aggregation due to the repulsive interaction. As a result, many Ag^{MON}-C bonds are broken before formation of Pd clusters. With increasing Pd coverage, Pd clusters grow from the unconnected lobes.

4. Conclusions

~~We succeeded in distributing Ag, In, and Pd clusters on a flat Ag substrate by capturing Ag, In, and Pd adatoms with the porous 2D-MON.~~ Our results show that Ag, In and Pd clusters grow in different ways in the 2D-MON and the interaction between the adatoms and the 2D-MON must be considered to clarify the growth mechanism. Regardless of the structure of the pore of the 2D-MON, the interaction is the key to determining the type of cluster growth. The attractive and repulsive interactions between the adatoms and the 2D-MON result in cluster growth on the 2D-MON and inside of the pores, respectively. Although the candidates for the interaction between the adatoms and the 2D-MON are the van der Waals and Coulomb interactions, more detailed considerations, such as the influence of the substrate, are necessary to clarify the details of the interaction for metal adatoms.

As discussed in the introduction, metal clusters are expected to have a particularly wide range of applications. By distributing magnetic atoms and clusters, we expect that metal clusters are a basic model for atomic-scale magnetic recording devices. In addition, heterogeneous catalysts are expected by distributing atoms and clusters with high catalytic activity. The preparation of a periodic potential well on the substrate is one of the promising ways to arrange metal clusters such as in our present study.

Acknowledgments

This work is supported by JST CREST (No. PMJCR20R4)), JSPS KAKENHI Grand Number 22H01960 and the association for the advancement of Science & Technology, Gunma University. RA gratefully acknowledge significant financial supports from the World Premier International Research Center Initiative (WPI) on Materials Nanoarchitectonics (MANA). The STM/STS measurements were performed by the joint research in The Institute for Solid State Physics, The University of Tokyo. The authors thank the Supercomputer Center, The Institute for Solid State Physics, The University of Tokyo, for the use of the facilities. A part of the DFT calculations were performed by using the computer facilities of National Institute for Materials Science (Numerical Material Simulator Station).

References

1) L. Dong, Z.A. Gao, and N. Lin, Prog. Surf. Sci. **91**(3), 101–135 (2016).
2) R. Sakamoto, K. Takada, T. Pal, H. Maeda, T. Kambe, and H. Nishihara, Chem. Commun. **53**(43), 5781–5801 (2017).
3) A. Dmitriev, H. Spillmann, N. Lin, J. V. Barth, and K. Kern, Angew. Chemie - Int. Ed. **42**(23), 2670–2673 (2003).
4) S. L. Tait, A. Langner, N. Lin, S. Stepanow, C. Rajadurai, M. Ruben, and K. Kern, J. Phys. Chem. C **111**(29), 10982–10987 (2007).
5) G. Pawin, K.L. Wong, D. Kim, D. Sun, L. Bartels, S. Hong, T.S. Rahman, R. Carp, and M. Marsella, Angew. Chemie - Int. Ed. **47**(44), 8442–8445 (2008).
6) M. Matena, M. Stöhr, T. Riehm, J. Björk, S. Martens, M.S. Dyer, M. Persson, J. Lobo-Checa, K. Müller, M. Enache, H. Wadepohl, J. Zegenhagen, T.A. Jung, and L.H. Gade, Chem. - A Eur. J. **16**(7), 2079–2091 (2010).
7) Z. Shi, J. Liu, T. Lin, F. Xia, P.N. Liu, and N. Lin, J. Am. Chem. Soc. **133**(16), 6150–6153 (2011).
8) J. Liu, T. Lin, Z. Shi, F. Xia, L. Dong, P.N. Liu, and N. Lin, J. Am. Chem. Soc. **133**(46), 18760–18766 (2011).
9) W. Wang, X. Shi, S. Wang, J. Liu, M.A. Van Hove, P.N. Liu, R.Q. Zhang, and N. Lin, Phys. Rev. Lett. **110**(4), 046802 (2013).
10) T.R. Umbach, M. Bernien, C.F. Hermanns, L.L. Sun, H. Mohrmann, K.E. Hermann, A. Krüger, N. Krane, Z. Yang, F. Nickel, Y.M. Chang, K.J. Franke, J.I. Pascual, and W. Kuch, Phys. Rev. B - Condens. Matter Mater. Phys. **89**(23), 235409 (2014).
11) S. Clair, and D.G. De Oteyza, Chem. Rev. **119**(7), 4717–4776 (2019).
12) C. J. Judd, S.L. Haddow, N.R. Champness, and A. Saywell, Sci. Rep. **7**(1), 14541 (2017).
13) D. Kühne, F. Klappenberger, R. Decker, U. Schlickum, H. Brune, S. Klyatskaya, M. Ruben, and J. V. Barth, J. Am. Chem. Soc. **131**(11), 3881–3883 (2009).
14) A. Kumar, K. Banerjee, A.S. Foster, and P. Liljeroth, Nano Lett. **18**(9), 5596–5602 (2018).
15) R. Zhang, J. Liu, Y. Gao, M. Hua, B. Xia, P. Knecht, A.C. Papageorgiou, J. Reichert, J. V. Barth, H. Xu, L. Huang, and N. Lin, Angew. Chemie - Int. Ed. **59**(7), 2669–2673 (2020).
16) Z. Yang, T. Sander, J. Gebhardt, T.A. Schaub, J. Schönamsgruber, H.R. Soni, A. Görling, M. Kivala, and S. Maier, ACS Nano **14**(12), 16887–16896 (2020).
17) W. Jiang, X. Ni, and F. Liu, Acc. Chem. Res. **54**(2), 416–426 (2021).

18) P. Gambardella, S. Stepanow, A. Dmitriev, J. Honolka, F.M.F. De Groot, M. Lingenfelder, S. Sen Gupta, D.D. Sarma, P. Bencok, S. Stanescu, S. Clair, S. Pons, N. Lin, A.P. Seitsonen, H. Brune, J. V. Barth, and K. Kern, Nat. Mater. **8**(3), 189–193 (2009).
19) N. Abdurakhmanova, T.C. Tseng, A. Langner, C.S. Kley, V. Sessi, S. Stepanow, and K. Kern, Phys. Rev. Lett. **110**, 027202 (2013).
20) T. Lin, G. Kuang, W. Wang, and N. Lin, ACS Nano **8**(8), 8310–8316 (2014).
21) T.R. Umbach, M. Bernien, C.F. Hermanns, A. Krüger, V. Sessi, I. Fernandez-Torrente, P. Stoll, J.I. Pascual, K.J. Franke, and W. Kuch, Phys. Rev. Lett. **109**(26), 1267207 (2012).
22) D. Grumelli, B. Wurster, S. Stepanow, and K. Kern, Nat. Commun. **4**, 2904 (2013).
23) F. Klappenberger, D. Kühne, W. Krenner, I. Silanes, A. Arnau, F.J. García De Abajo, S. Klyatskaya, M. Ruben, and J. V. Barth, Phys. Rev. Lett. **106**(2), 026802 (2011).
24) M. Pivetta, G.E. Pacchioni, U. Schlickum, J. V. Barth, and H. Brune, Phys. Rev. Lett. **110**(8), 086102 (2013).
25) I. Piquero-Zulaica, A. Sadeghi, M. Kherelden, M. Hua, J. Liu, G. Kuang, L. Yan, J.E. Ortega, Z.M.A. El-Fattah, B. Azizi, N. Lin, and J. Lobo-Checa, Phys. Rev. Lett. **123**(26), 266805 (2019).
26) I. Piquero-Zulaica, Z.M. Abd El-Fattah, O. Popova, S. Kawai, S. Nowakowska, M. Matena, M. Enache, M. Stöhr, A. Tejeda, A. Taleb, E. Meyer, J.E. Ortega, L.H. Gade, T.A. Jung, and J. Lobo-Checa, New J. Phys. **21**(5), 053004 (2019).
27) D. Kühne, F. Klappenberger, W. Krenner, S. Klyatskaya, M. Ruben, and J. V. Barth, Proc. Natl. Acad. Sci. U. S. A. **107**(50), 21332–21336 (2010).
28) C.A. Palma, J. Björk, F. Klappenberger, E. Arras, D. Kühne, S. Stafström, and J. V. Barth, Nat. Commun. **6**, 6210 (2015).
29) U. Schlickum, R. Decker, F. Klappenberger, G. Zoppellaro, and S. Klyatskaya, Nano Lett. **12**, 3813–3817 (2007).
30) Q. Zhang, G. Kuang, R. Pang, X. Shi, and N. Lin, ACS Nano **9**(12), 12521–12528 (2015).
31) R. Zhang, G. Lyu, C. Chen, T. Lin, J. Liu, P.N. Liu, and N. Lin, ACS Nano **9**(8), 8547–8553 (2015).
32) A.T. N'Diaye, S. Bleikamp, P.J. Feibelman, and T. Michely, Phys. Rev. Lett. **97**(21), 215501 (2006).
33) Z. Zhou, F. Gao, and D.W. Goodman, Surf. Sci. **604**(13–14), L31–L38 (2010).
34) E. Sutter, P. Albrecht, B. Wang, M.L. Bocquet, L. Wu, Y. Zhu, and P. Sutter, Surf. Sci. **605**(17–18), 1676–1684 (2011).

35) B. Wang, B. Yoon, M. König, Y. Fukamori, F. Esch, U. Heiz, and U. Landman, Nano Lett. **12**(11), 5907–5912 (2012).
36) M. Sicot, P. Leicht, A. Zusan, S. Bouvron, O. Zander, M. Weser, Y.S. Dedkov, K. Horn, and M. Fonin, ACS Nano **6**(1), 151–158 (2012).
37) B. Wang, and M.L. Bocquet, J. Phys. Chem. Lett. **2**(18), 2341–2345 (2011).
38) E. Sutter, B. Wang, P. Albrecht, J. Lahiri, M.L. Bocquet, and P. Sutter, J. Phys. Condens. Matter **24**(31), 314201 (2012).
39) N. Tsukahara, and J. Yoshinobu, Langmuir **38**(29), 8881–8889 (2022).
40) G. Kresse, and J. Furthmüller, Phys. Rev. B **54**(16), 4053–4061 (1996).
41) P.E. Blöchl, Phys. Rev. B **50**(24), 17953–17979 (1994).
42) J. Klime, D.R. Bowler, and A. Michaelides, Phys. Rev. B - Condens. Matter Mater. Phys. **83**(19), 195131 (2011).
43) R. Gutzler, H. Walch, G. Eder, S. Kloft, W.M. Heckl, and M. Lackinger, Chem. Commun. (29), 4456–4458 (2009).
44) J. Eichhorn, T. Strunskus, A. Rastgoo-Lahrood, D. Samanta, M. Schmittel, and M. Lackinger, Chem. Commun. **50**(57), 7680–7682 (2014).
45) M. Fritton, K. Otte, J. Björk, P.K. Biswas, W.M. Heckl, M. Schmittel, and M. Lackinger, Chem. Commun. **54**(70), 9745–9748 (2018).
46) C.M. Doyle, C. McGuinness, A.P. Lawless, A.B. Preobrajenski, N.A. Vinogradov, and A.A. Cafolla, Phys. Status Solidi Basic Res. **256**(2), 1800349 (2019).
47) C.J. Judd, F.L.Q. Junqueira, S.L. Haddow, N.R. Champness, D.A. Duncan, R.G. Jones, and A. Saywell, Commun. Chem. **3**(1), (2020).
48) J. Hu, J. Hu, Z. Zhang, K. Shen, Z. Liang, H. Zhang, Q. Tian, P. Wang, Z. Jiang, H. Huang, J.W. Wells, and F. Song, Appl. Surf. Sci. **513**(October 2019), 145797 (2020).
49) G. Henkelman, A. Arnaldsson, and H. Jónsson, Comput. Mater. Sci. **36**(3), 354–360 (2006).
50) E. Sanville, S.D. Kenny, R. Smith, and G. Henkelman, J. Comput. Chem. **28**(5), 899–908 (2007).
51) W. Tang, E. Sanville, and G. Henkelman, J. Phys. Condens. Matter **21**(8), (2009).
52) M. Yu, and D.R. Trinkle, J. Chem. Phys. **134**(6), (2011).
53) M. Dion, H. Rydberg, E. Schröder, D.C. Langreth, and B.I. Lundqvist, Phys. Rev. Lett. **92**(24), 22–25 (2004).
54) R. M. Ferullo, N.F. Domancich, and N.J. Castellani, Chem. Phys. Lett. **500**(4–6), 283–286 (2010).

55) F. P. Novais Antunes, V. S. Vaiss, S.R. Tavares, R.B. Capaz, and A.A. Leitão, Comput. Mater. Sci. **152**, 146–150 (2018).
56) D.C. Ghosh, and R. Biswas, Int. J. Mol. Sci. **3**(2), 87–113 (2002).

Figure Captions

Fig. 1. (a) STM image of the 1.0 ML TBB molecules on Ag(111) after heating the substrate. V_s = -1.5 V, I_t = 10 pA, 15 nm × 15 nm, and T = 78 K. (b) Line profiles along the black lines (lines 1 and 2) in (a). (c) Schematic drawings of the 2D-MON along lines 1 and 2. (d) Line profiles along the black lines (lines 3 and 4) in (a). (e) Schematic drawings of the expected structure of the unconnected molecular lobes along lines 3 and 4. (f) An enlarged STM image in the dotted square in (a) and a schematic drawing of the 2D-MON in the enlarged image. The drawing assumes that the termination of the longer lobe is connected with a Br atom. (g) and (h) Schematic drawings of the 2D-MON on Ag(111) after structural relaxation by DFT calculation, (g) top view, (h) side view.

Fig. 2. (a) An STM image of the 2D-MON after the deposition of Ag atoms. The deposition rate and time are 0.03 Å/s and 5 sec, respectively. V_s = -0.5 V, I_t = 10 pA, 20 nm × 20 nm, and T = 78 K. (b) An STM image of the 2D-MON after the deposition of In atoms. The deposition rate and time are 0.015 Å/s and 8 sec, respectively. V_s = -2.0 V, I_t = 10 pA, 15 nm × 15 nm, and T = 78 K. (c) An STM image of the 2D-MON after the deposition of Pd atoms. The deposition rate and time are 0.025 Å/s and 3 sec, respectively. V_s = -1.5 V, I_t = 10 pA, 20 nm × 20 nm, and T = 78 K. (d) to (f) Line profiles of α, β, and γ clusters shown with an underline in (a). (g) and (h) Line profiles of β, and γ clusters shown with an underline in (b). (i) A Line profile of the Pd cluster shown in the inset.

Fig. 3. (a) and (b) Enlarged STM images of an Ag and In adatoms on the 2D-MON in Figs. (a) and (b). Schematic drawings of the expected adsorption sites. The adatoms moves by scanning.

Fig. 3. (a) An STM image of the 2D-MON after the deposition of In atoms. The deposition rate and time are 0.015 Å/s and 8 sec, respectively. V_s = -2.0 V, I_t = 10 pA, 15 nm × 15 nm, and T = 78 K. (b) and (c) Line profiles of β, and γ clusters shown with an underline in (a).

(d) An enlarged STM image of an In adatom on the 2D-MON in Fig. 3 (a) and a schematic drawing of the expected adsorption site. (e) Enlarged STM images of an Ag adatom on the 2D-MON in Fig. 2 (a) and a schematic drawing of the expected adsorption site. The Ag adatom moves to neighboring adsorption site by scanning.

Fig. 4. (a) An STM image of the 2D-MON after the deposition of Pd atoms. The deposition rate and time are 0.025 Å/s and 3 sec, respectively. V_s = -1.5 V, I_t = 10 pA, 20 nm × 20 nm, and T = 78 K. (b) A Line profile of the Pd cluster shown in the inset. (c) Line profiles along lines 5 and 6 as shown in the inset. (d) A schematic drawing of an Ag or Pd atom bonded to two phenyl rings. (e) A schematic drawing of the Pd adatom that reaches Ag^{MON}.

Fig. 4. (a) Labels of the adsorption sites for Ag, In, and Pd adatoms. (b) to (d) Total energies of the 2D-MON on Ag(111) with the Ag, In, and Pd adatoms at the positions shown in (a), respectively. Zero on the vertical axis is the energy when each atom is positioned at site A. (e) Projected density of states (PDOS) of Ag^{MON} when no Ag adatoms in a pore. PDOS of an Ag adatom on Ag(111) is also shown. (f) PDOS of Ag^{MON} when an Ag adatom is at site K. PDOS of an Ag adatom at site K is also shown.

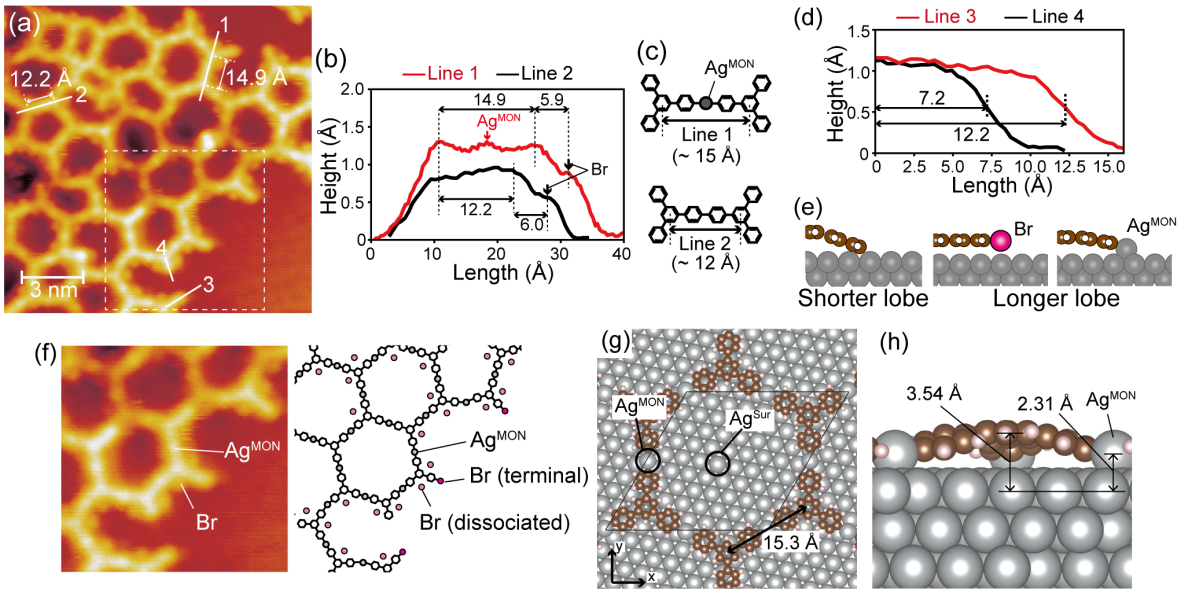
(a)
12.2 Å
14.9 Å
1
2
3
4
3 nm
(b)
Line 1
Line 2
14.9
5.9
Ag^MON
Br
12.2
6.0
Height (Å)
Length (Å)
(c)
Ag^MON
Line 1
(~ 15 Å)
Line 2
(~ 12 Å)
(d)
Line 3
Line 4
7.2
12.2
Height (Å)
Length (Å)
(e)
Br
Ag^MON
Shorter lobe
Longer lobe
(f)
Ag^MON
Br
Br (terminal)
Br (dissociated)
(g)
Ag^MON
Ag^Sur
15.3 Å
y
x
(h)
3.54 Å
2.31 Å
Ag^MON

Fig. 1.

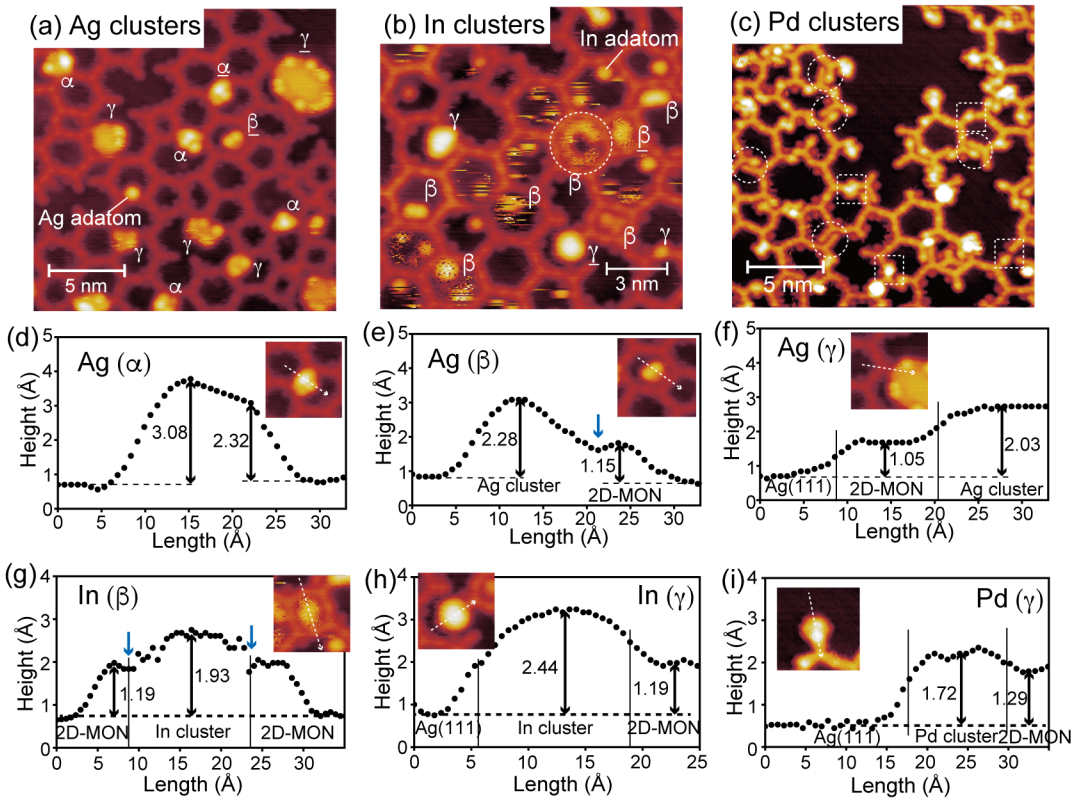
(a) Ag clusters
Ag adatom
5 nm
(b) In clusters
In adatom
3 nm
(c) Pd clusters
5 nm
(d) Ag (α)
3.08
2.32
(e) Ag (β)
2.28
1.15
Ag cluster
2D-MON
(f) Ag (γ)
1.05
2.03
Ag(111)
2D-MON
Ag cluster
(g) In (β)
1.19
1.93
2D-MON
In cluster
2D-MON
(h) In (γ)
2.44
1.19
Ag(111)
In cluster
2D-MON
(i) Pd (γ)
1.72
1.29
Ag(111)
Pd cluster
2D-MON
Height (Å)
Length (Å)

Fig. 2.

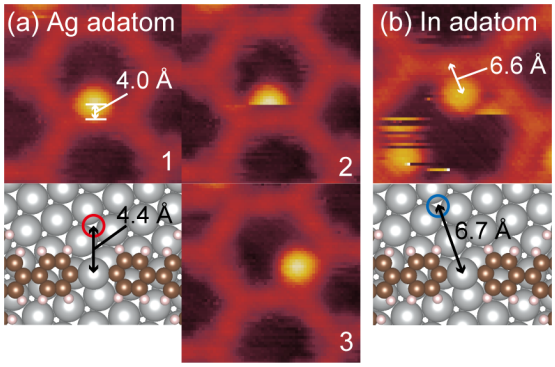

Fig. 3

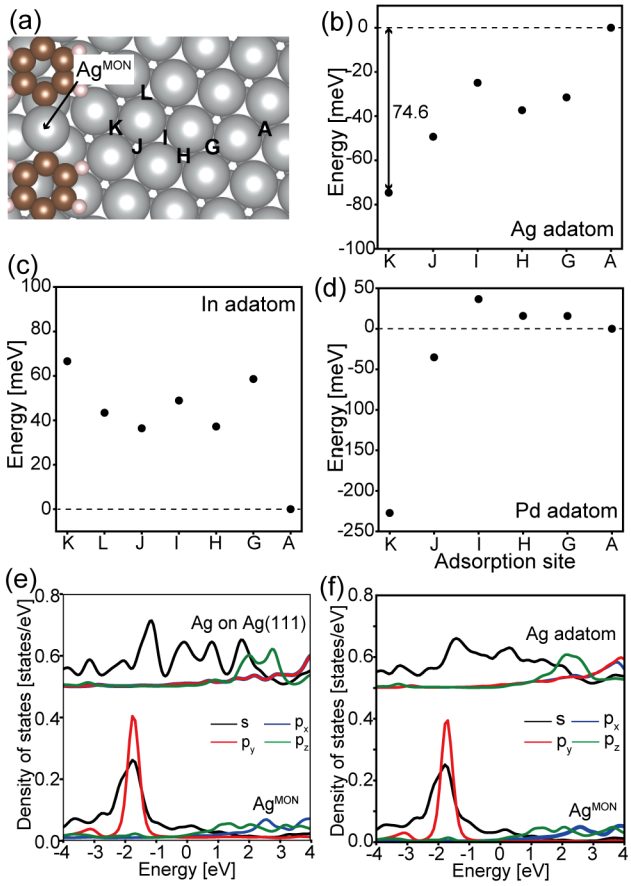
(a)
Ag^MON
L
K
J
I
H
G
A
(b)
Energy [meV]
74.6
Ag adatom
K J I H G A
(c)
In adatom
Energy [meV]
K L J I H G A
(d)
Energy [meV]
Pd adatom
K J I H G A
Adsorption site
(e)
Ag on Ag(111)
Density of states [states/eV]
s
p_x
p_y
p_z
Ag^MON
Energy [eV]
(f)
Ag adatom
Density of states [states/eV]
s
p_x
p_y
p_z
Ag^MON
Energy [eV]

Fig. 4.